Modeling intrinsic defects in $LiNbO_3$ within the Slater-Janak transition state model

Yanlu Li,[a] Simone Sanna, and Wolf Gero Schmidt
Lehrstuhl für Theoretische Physik, Universität Paderborn, 33095 Paderborn, Germany

(Received 24 March 2014; accepted 4 June 2014; published online 19 June 2014)

Intrinsic point defects in $LiNbO_3$, i.e., isolated Nb antisites and Li as well Nb vacancies, are investigated from first-principles within the Slater-Janak transition state model. Thereby the electronic structure of the investigated defects is calculated with hybrid exchange-correlation functionals. This approach allows for the calculation of charge transition levels without comparing the total energies of differently charged supercells. The obtained results are in agreement with previous hybrid density-functional theory calculations based on total-energy differences. Li and Nb vacancies can be formed in the V_{Li}^{-} and V_{Nb}^{5-} charge states only, as long as the host is not strongly *p*-type or *n*-type, respectively. Nb_{Li} antisites may capture one or two electrons, forming the defect states often referred to as small bound polaron and bi-polaron. © *2014 AIP Publishing LLC*. [http://dx.doi.org/10.1063/1.4883737]

Lithium niobate ($LiNbO_3$, LN) is an important technological material with outstanding ferroelectric, piezoelectric, photorefractive, and electro-optical properties,[1] which finds applications in optical waveguides, piezoelectric sensors, optical modulators, and various other linear and nonlinear optical devices. Understanding the LN defect structure is important, as many of its properties, such as the extraordinary refractive index, the optical absorption, the linear electro-optical effect, and the birefringence are strongly influenced by, or even due to, point defects.[2–6]

Experimentally[7–10] a high degree of ionic disorder and Li_2O deficiency is found for most LN crystals. In particular there are numerous Nb antisite (Nb_{Li}) defects,[7–9] which might be charge compensated either by Nb vacancies (V_{Nb}) in the Nb vacancy model[8] or by Li vacancies (V_{Li}) in the Li vacancy model.[11] Wilkinson and co-workers[12] pointed out that the growth conditions determine the degree of filling of Li sites by Nb ions. Thus all three defects Nb_{Li}, V_{Li}, and V_{Nb} may coexist in congruent crystals.

On the theoretical side, Nahm and Park[13] investigated the electronic properties of Nb antisites with local-density approximation (LDA) plus Hubbard *U* (LDA+*U*), confirming the negative *U* behavior predicted by Schirmer *et al.*[14] Donnerberg *et al.*[15] found Li vacancies energetically preferable over Nb vacancies for the compensation of Nb antisites. This agrees with two *ab initio* studies[16,17] that concluded that the lithium-vacancy model is the most probable LN defect model. A more recent study[18] by the present authors, where finite-size effects were given particular attention found, however, that Nb antisites, Li, and Nb vacancies may coexist in congruent LN samples.

The defect formation energies (DFEs) and charge transition levels (CTLs) available in the literature vary over a sizeable range. Furthermore, different charge states are reported. The most striking example is given by the Nb vacancy, which is predicted to be either neutral[16] or threefold negatively charged[17] for Fermi energies in the lower part of the band gap. Thus, a conclusive theoretical picture of the intrinsic defects characterizing congruent $LiNbO_3$ is still missing. This is due, on turn, to the various challenges in the modeling of point defects within density-functional theory (DFT). The calculations typically rest on periodic boundary conditions (PBC) and are thus plagued by problems due to the interaction of the defect with its periodic images.[19–24] This affects the calculation of DFEs and CTLs, which turn out to be strongly dependent on the size of the supercell. Considering again V_{Nb}^{5-} as an example, Li *et al.*,[17] calculate its formation energies to be −114 and 13 eV using supercells containing 80 and 180 atoms, respectively.

In the present work the structural and electronic properties of the most relevant intrinsic LN point defects Nb_{Li}, V_{Li}, and V_{Nb} (see Fig. 1) are studied in the framework of the density-functional theory, using local and hybrid exchange-correlation (XC) potentials. Thereby charge transition levels are not obtained from total-energy differences, but calculated using the Slater-Janak (SJ) transition state model. The calculated CTLs are in agreement with the outcome of recent hybrid-DFT calculations based on total energy differences.[18] Thus, the Slater-Janak approach represents a viable alternative to established calculation schemes in computational defect physics. The negative *U* behavior of Nb_{Li} antisites is correctly reproduced. Li and Nb vacancies are likely formed in the −1 and −5 charge states, respectively.

The present calculations employ the Vienna *ab initio* Simulation Package (VASP)[25,26] implementation of DFT in conjunction with the projector-augmented-wave (PAW) formalism.[27] Plane waves up to a cutoff energy of 400 eV form the basis set for the wave function expansion. The defect geometries are modeled using the Perdew-Burke-Ernzerhof (PBE) formulation of the generalized gradient approximation (GGA), accounting for spin polarization. Thereby hexagonal 2 × 2 × 1 supercells containing 120 atoms are employed. A 4 × 4 × 4 Monkhorst-Pack mesh[28] samples the

[a]yanlu.li@upb.de

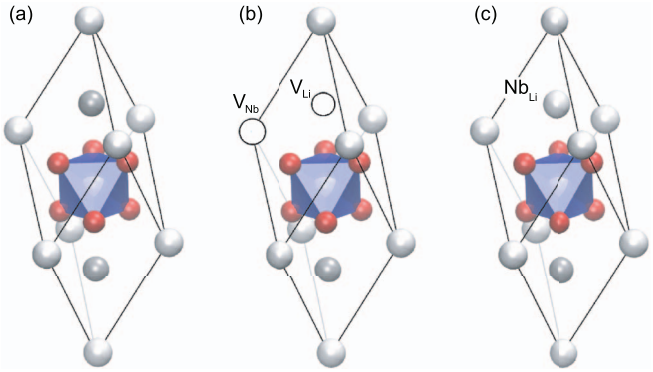

FIG. 1. Ball and stick models for defect free $LiNbO_3$ (a). V_{Li} and V_{Nb} are formed removing a single Li (in gray) and Nb atom (in white) (b). Nb_{Li} are formed substituting one Li ion by a Nb (c).

Brillouin zone. The atomic positions within the supercells are relaxed until the Hellmann-Feynman forces acting on the single ions are lower than 0.01 eV/Å. Further convergence tests are performed, for computational reasons, within the local PBE functional with larger hexagonal supercells containing 240 and 480 atoms, and with rhombohedral 2 × 2 × 2 and 3 × 3 × 4 supercells containing 80 and 360 atoms, respectively. While geometry and electronic structure of V_{Li} and Nb_{Li} are converged within 120 atoms cells, larger cells are required to model V_{Nb}.[18] The finite size error in the calculation of the V_{Nb} DFE amounts to about 0.35 eV. Hybrid-functional calculations are performed using the HSE06 functional,[29,30] where 25% of the local PBE exchange is substituted by exact exchange. Thereby 2 × 2 × 2 Monkhorst-Pack meshes and the GGA geometry are used. The application of hybrid potentials opens the nearly direct electronic band gap from 3.53 eV to 5.21 eV, in agreement with earlier quasiparticle calculations.[31]

The defect formation energy and the charge transition levels are typically determined as a function of the Fermi level position from total energy differences:[21,32]

$$E_f(X^q) = E^{total}(X^q) - \sum_i n_i \mu_i + q E_F. \qquad (1)$$

Here $E^{\text{total}}(X^q)$ is the total energy derived from a supercell with defect X, n_i indicates the number of atoms of species, i and μ_i are the corresponding chemical potentials. E_F is the Fermi level with respect to the bulk valence band maximum (VBM). Unfortunately, the total energy of a charged supercell converges slowly with the cell size, so that several energy correction schemes are usually applied to overcome this issue.[19–24] However, the correction schemes are themselves an approximation and are not universally applicable.[33] The SJ transition state model is an alternative method to determine CTLs within DFT, which is successfully applied, among others, to wide gap systems.[34,35] This method does not require to compare the total energies of differently charged systems and is therefore less affected from issues arising from the supercell approach. The Kohn-Sham eigenvalues are related to the derivative of the total energy E with respect to the occupation number η_i of the respective orbital,[36]

$$\frac{\partial E[N]}{\partial \eta_i} = \varepsilon_i. \qquad (2)$$

Here ε_i is the Kohn-Sham eigenvalue of the ith orbital. Assuming that the Kohn-Sham eigenvalue of the highest occupied state ε_H varies linearly with its occupation number, the SJ transition state can be defined via

$$E^{N+1} - E^N = \int_0^1 \varepsilon_H(\eta) d\eta = \varepsilon_H\left(\frac{1}{2}\right), \qquad (3)$$

where E^{N+1} and E^N are the energies of the $N+1$ and N electron systems, respectively. Typically, $\varepsilon_H(\frac{1}{2})$ can be estimated from the average of the eigenvalues of the lowest unoccupied orbital in the N electron system and the highest occupied orbital in the $N+1$ electron system. This method requires the linear dependence of ε_H on the occupation number. This condition is, with exception of strongly correlated systems,[37] generally fulfilled, as shown by Goransson,[38] since the Kohn-Sham eigenvalues depend in first approximation linearly on their occupation number.

In order to refer to the equilibrium, i.e., force free geometry for the system with the HOMO occupation $\eta = 0.5$ within the Slater-Janak transition-state, the corresponding structure determination is indeed performed with a half occupied electronic level. This configuration does not describe any physical defect state, however. It only provides the correct position of the electronic charge transition within the fundamental band gap. The geometry and charge distribution of the actual defect states discussed below are, in contrast, calculated for integer occupations.

The choice of the supercell size requires to find a good compromise between accuracy and computational costs. While a 2 × 2 × 2 repetition of the rhombohedral $LiNbO_3$ unit cell contains 80 atoms, a 3 × 3 × 3 supercell contains 270 atoms and a 4 × 4 × 4 supercell 640. In order to use supercells containing a number of atoms in between 270 and 640, for example, a 3 × 3 × 4 supercell with 360 atoms could be used. However, not only the size of the supercell, also its symmetry is important for a correct description of the defect properties. LN is polarized along the [111] direction, which is also the three-fold rotation axis that characterizes the C_3 symmetry of the defects studied here. Using rhombohedral supercells with a different number of repetition units the threefold rotation axis does not coincide with the [111] direction, thus supercell and crystal lattice are characterized by a different symmetry (see Fig. 2). As explained in Ref. 39, this artificial symmetry breaking has a noticeable influence on the calculated formation energies. The discrepancies are particularly severe in case of the Nb vacancy. As an example, the formation energy of the neutral V_{Nb} calculated by total energy differences amounts to about 5 eV using a 3 × 3 × 4 rhombohedral cell, while it is about 2 eV higher if calculated with homogeneous rhombohedral or hexagonal supercells. In hexagonal supercells the polarization axis is parallel to the threefold rotation axis, irrespective of the number of unit of repetition. The sensitivity of the V_{Nb} results with respect to the application of PBCs confirms earlier findings[16,17] and explains in part the scatter in the literature results. In order not to break the symmetry due to PBCs, hexagonal unit cells are used throughout this work.

Based on the hexagonal 120 atoms unit cells as discussed above, and using hybrid functionals to calculate the electronic

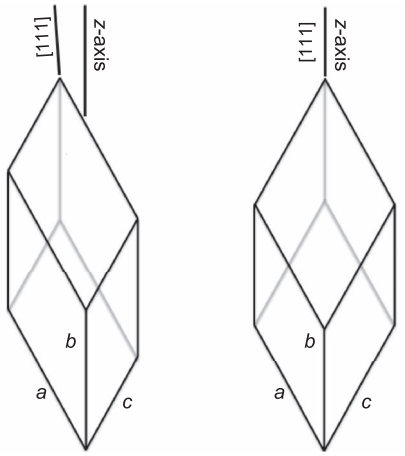

FIG. 2. While in a $a \times b \times c$ repetition of the rhombohedral $LiNbO_3$ primitive cell with $a = b = c$ the crystallographic [111] axis coincides with the polarization axis and the threefold rotation axis (right hand side), this is not the case if $a \neq b \neq c$ (left hand side).

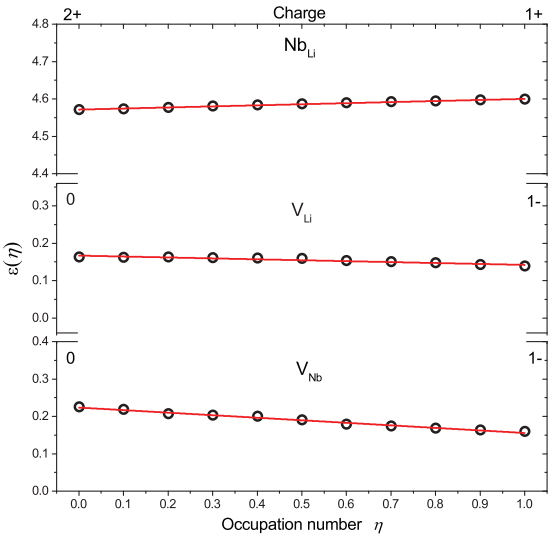

FIG. 3. Energy (in eV) of the highest occupied one-particle levels as a function of their occupation numbers for Nb_{Li}^{2+}, V_{Li}^{-}, and V_{Nb}^{-} in LN. The energy zero corresponds to the VBM.

structure of the system, we determine the CTLs within the SJ transition state model. The potential correction described by Eq. (20) of Ref. 23 is applied in order to account for the effect of charged supercells on the one-particle levels. Thereby, the weighted average of the experimental values of the static dielectric tensor components $\varepsilon_s^{11} = 84$ and $\varepsilon_s^{33} = 29$ given in Ref. 42 are used. We only consider the leading correction term, as higher order terms result in contributions of few meV. Due to the high dielectric constant of $LiNbO_3$ (i.e., efficient screening effects) the corrections generally amount to few hundredth of 1 eV. Only in case of highly charge states such as V_{Nb}^{5-} the charge corrections reach up to the tenth of eV.

The condition underlying these calculations, i.e., the linearity of the Kohn-Sham eigenvalues in dependence on the respective occupation numbers is well satisfied, as exemplarily shown for Nb_{Li}^{2+}, V_{Li}^{-}, and V_{Nb}^{-} in Fig. 3. The figure shows that the considered one-particle levels are a linear, nearly constant function of the occupation numbers. The magnitude of the slopes is lower than 0.07 eV/e in all the considered cases. This is not the case if local XC potentials are applied, resulting in a strongly convex function for total energy vs occupation, in particular in the case of Nb_{Li}. This a known drawback of GGA functionals, related to too strongly delocalized electronic wave functions, so that polaronic effects might be missed. Thus, the application of non-local XC-functionals becomes crucial for the correct modeling of Nb_{Li} antisites.

The SJ transition levels calculated with respect to the VBM are compiled in Table I. The upper part shows the predicted charge state transition energies, while the lower part shows hypothetical transitions involving unstable configurations. In Fig. 4 the CTLs compiled in Table I are graphically compared to the CTLs calculated via total-energy differences, using the same computational parameters (also corresponding to the approach in Ref. 18) and applying the charge correction scheme proposed in Ref. 20. As in the case of the potential correction, only the leading term – i.e., the monopole contribution – is considered, as the quadrupole term is an order of magnitude smaller. The formation energy of the neutral charge state is used as reference. Particular attention must be paid to the notation in the case of the niobium antisite. The isolated Nb ion (Nb^0, $[Kr]4d^45s^1$) has five valence electrons.

TABLE I. Slater-Janak transition model calculations for Nb_{Li}, V_{Li}, and V_{Nb} CTLs. All the values are in eV above the VBM. The calculated band gap amounts to 5.21 eV.

Nb_{Li}		V_{Li}		V_{Nb}	
$\varepsilon(5^+/3^+)$	4.16	$\varepsilon(0/1^-)$	0.21	$\varepsilon(0/1^-)$	0.22
$\varepsilon(3^+/2^+)$	4.52	$\varepsilon(1^-/3^-)$	4.99	$\varepsilon(1^-/2^-)$	0.47
$\varepsilon(2^+/1^+)$	4.54			$\varepsilon(2^-/3^-)$	0.62
				$\varepsilon(3^-/5^-)$	0.89
$\varepsilon(5^+/4^+)$	4.16	$\varepsilon(1^-/2^-)$	5.01	$\varepsilon(3^-/4^-)$	0.92
$\varepsilon(4^+/3^+)$	4.15	$\varepsilon(2^-/3^-)$	4.98	$\varepsilon(4^-/5^-)$	0.87

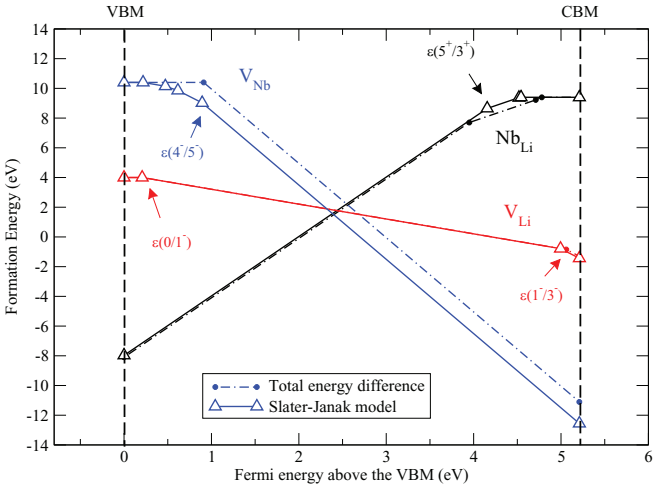

FIG. 4. Defect formation energies of Nb_{Li}, V_{Li}, and V_{Nb} in LN calculated with the Slater-Janak transition state model (solid lines) and by total-energy differences (dashed lines) as a function of Fermi energy.

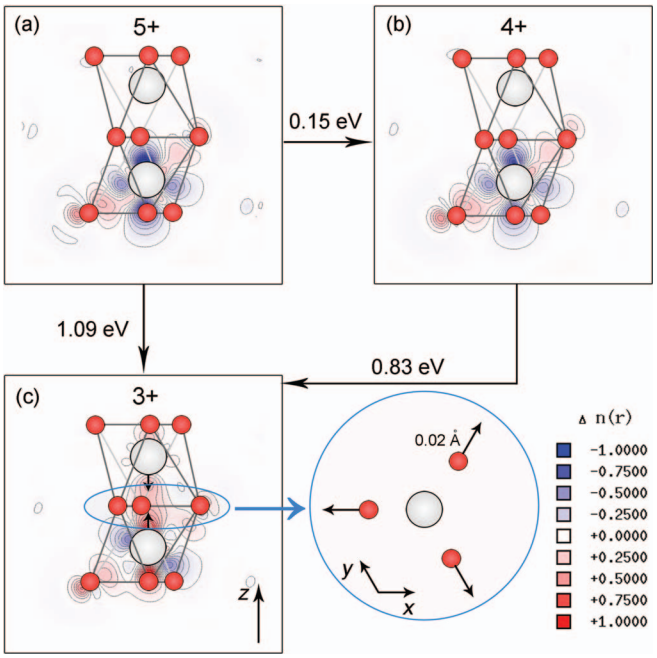

FIG. 5. [(a)–(c)] Electron density difference for different charge states of the antisite Nb_{Li} along a $(2\bar{1}\bar{1}0)$ plane. Blue and red regions represent electron depletion and accumulation, respectively. Arrows between the boxes indicate the relaxation energy. Atomic color coding as in Fig. 1.

When it is incorporated in the host as an antisite, it substitutes a ionized lithium (Li^+), and one of valence electrons is promoted to the host to form the ionic bond (Nb^+, $[Kr]4d^45s^0$). Thus, a fourfold charged supercell models a fivefold charged substitutional (Nb^{5+}, $[Kr]4d^05s^0$). This explains the different notation used, e.g., in Ref. 13, and in Refs. 16 and 18 to identify the same charge state. In this work we adopt the notation of Ref. 13, which differs from our previous work.[18]

The antisite Nb_{Li} occurs as fivefold positive defect Nb_{Li}^{5+} for values of the electron chemical potential below 4.16 eV. The associated lattice relaxation energy amounts to 5.37 eV (Fig. 5(a)). In this charge state (outer electronic configuration $[Kr]4d^05s^0$) the defect can host one electron, corresponding to Nb_{Li}^{4+} ($[Kr]4d^15s^0$). The transition causes a large structural relaxation that lowers the energy by further 0.15 eV and contributes to localize the electron at the defect. This object is usually referred to as small bound polaron (Fig. 5(b)). However, the charge transition $\varepsilon(4^+/3^+)$ occurs before the $\varepsilon(5^+/4^+)$ transition ($\Delta\varepsilon = 0.01$ eV), indicating the negative-U behavior of the defect and resulting in a $\varepsilon(5^+/3^+)$ transition at 4.16 eV above the VBM. In this configuration (Nb_{Li}^{3+}) the structural relaxation is even more pronounced than in the previous charge states and involves the next neighboring Nb along the crystal z-axis. The energy gain due to the structural relaxation of about 0.83 eV compensates the coulombic electron repulsion, favoring the negative-U behavior. Due to the mentioned relaxation, the Nb_{Li}^{3+} defect state is more appropriately represented by the $Nb_{Nb}^{4+} - Nb_{Li}^{4+}$ ($[Kr]4d^15s^0 - [Kr]4d^15s^0$) defect complex, usually referred to as a bound bipolaron (Fig. 5(c)). The charge transition $\varepsilon(5^+/3^+)$ occurring at 4.16 eV above the VBM is in agreement with the value calculated by total-energy differences at 3.95 eV. Further charge transitions to less charged defect states are expected

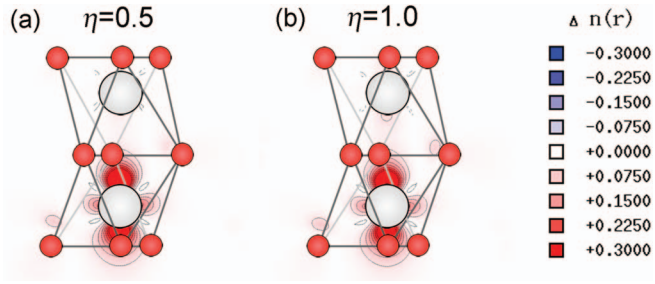

FIG. 6. [(a) and (b)] Squared wave function of the highest occupied electronic state of the antisite Nb_{Li}^{4+} along a $(2\bar{1}\bar{1}0)$ plane for occupations $\eta = 0.5$ and $\eta = 1$. Atomic color coding as in Fig. 1.

for higher values of the Fermi energy within the fundamental gap. The transitions $\varepsilon(3^+/2^+)$ and $\varepsilon(2^+/1^+)$ are calculated at 4.52 and 4.54 eV above the VBM, corresponding to the transitions calculated at 4.71 and 4.78 eV, respectively, via total-energy differences. However, as shown by Xu *et al.*,[16] these states are characterized by a high formation energy and are energetically unfavorable with respect to other defect structures.

Nahm and Park pointed out the necessity of an approach beyond DFT for an appropriate description of the Nb 4*d* orbitals and the correct modeling of the negative-U behavior of Nb_{Li} antisites. They applied an LDA+U calculation scheme to take into account the orbital dependence of the Coulomb and exchange interactions. The latter is absent in the LDA, resulting in too strongly delocalized *d* or *f* orbitals and the underestimation of polaronic effects. In order to prove the localization of the electronic wave function, we plot the squared wave function corresponding to the highest occupied electronic level of the Nb_{Li}^{4+} antisite in Fig. 6. It is clearly shown that the HOMO is strongly localized around the Nb substitutional, suggesting that the polaronic nature of the system is correctly reproduced within hybrid-functionals. Thus, our hybrid functional calculations within the SJ transition state mirror the LDA+U models of Ref. 13 and describe the bound polaron model proposed by Schirmer *et al.*[14] We are not aware of a direct measurement of the energetic position of the polaron states with respect to the $LiNbO_3$ bulk band edges. Therefore, the comparison of our results with the experiment is difficult. However, as pointed out by Nahm and Park,[13] the calculated defect states can be *indirectly* compared with several available measurements. The defect state associated to the small bound polaron $Nb_{Li}^{4+}(4d^1)$ is calculated in this work at 0.74 eV below the corresponding CBM, which is consistent with the binding energy of the small polaron estimated in 0.62 eV from conductivity measurements.[40] Similarly, the calculated difference between the defect levels of polaron $Nb_{Li}^{4+}(4d^1)$ and bipolaron $Nb_{Li}^{3+}(4d^2)$ of about 0.4 eV is indirectly comparable with the difference of 0.9 eV of the adsorption spectra peaks related to small bound polaron and bi-polaron.[41] A thorough discussion of the comparison between experimental data and the DFT model can be found in the original work of Nahm and Park.[13]

The lithium vacancy is characterized by a shallow $\varepsilon(0/1^-)$ transition at 0.21 eV above the valence band maximum and by a $\varepsilon(1^-/3^-)$ transition at 0.22 eV below the conduction band minimum, indicating that the dominant

charge state of the lithium vacancy in the singly negative charge state, which occurs as long as the material is not strongly *n*-type or strongly *p*-type. The V_{Li}^{-} vacancy does not result in a pronounced lattice relaxation. The structural relaxation lowers the system total energy by only 0.67 eV. Both the electronic charge distribution as well as the atomic configuration around the vacancy are very close to the undistorted configuration. As in the case of the Nb_{Li} antisite, the position of the charge transitions calculated with Slater-Janak model is in fair agreement with the CTLs calculated by total-energy differences. The $\varepsilon(0/1^{-})$ transition is calculated at 0.21 eV above the VBM both within the Slater-Janak model and by total energy differences. The double transition $\varepsilon(1^{-}/3^{-})$ is calculated at 4.99 and 5.06 eV above the VBM, respectively (see Fig. 4).

On the other end, the niobium vacancy gives rise to a large lattice rearrangement extended over several lattice sites, which lowers the system energy by 9.29 eV. The defect is characterized by a rapid succession of very close charge transitions from the neutral to the fivefold charged state ranging from 0.22 to 0.89 eV above the VBM. These appear as a single transition at 0.91 eV if the formation energy is calculated by total-energy differences. The uncommon fivefold transition resulting from total-energy differences might be due to the limitations of the charge correction schemes. However, both methods indicate that the niobium vacancy only exists in the fivefold negative charge state as long as the material is not *p*-type. Unfortunately, there are no experimental data that clarify the details of the V_{Nb} charge transitions for Fermi levels close to the VBM. The extremely different behavior of Li and Nb vacancies can be understood considering the atomic bonding in LN. Nb forms electronic bonds of mostly covalent character with the atoms of the surrounding oxygen octahedra. Thereby the five Nb valence electrons and the Li valence electrons are consumed. The resulting Li^{+} is fully ionized and highly mobile, thus when a V_{Li} is formed the structural relaxation is limited. Instead, when a V_{Nb} is formed several atomic bonds are broken and the resulting lattice rearrangement is substantial.

Summarizing, the antisite Nb_{Li} and the vacancy defects V_{Li} and V_{Nb} in lithium niobate have been investigated by hybrid density functional theory within the Slater-Janak transition state model. The results are largely in agreement with charge-corrected total-energy difference calculations, with minor deviations in the sequence of the V_{Nb} charge states close to the VBM. This shows on the one hand that the Slater-Janak transition state in combination with approaches improving the DFT description of the LN band gap such as hybrid potentials represents a viable alternative to total-energy difference calculations for the investigation of intrinsic and extrinsic point defects in LN. On the other hand, the present results corroborate earlier findings that for Fermi energies in the mid-gap region, Li and Nb vacancies occur exclusively in the charge states −1 and −5, respectively. Nb antisites may occur in the charge state +5 or capture one or two electrons to form small bound polarons or bi-polarons, depending on the position of the Fermi energy within the electronic band gap. This is of particular value given the large deviations in the previously reported DFT LN point defect energies and CTLs.

We gratefully acknowledge financial support from the DFG (TRR142 and SCHM1361/21) as well as supercomputer time provided by the HLRS Stuttgart.

[1] K. K. Wong, *Properties of Lithium Niobate* (INSPEC, Stevenage, Herts, UK, 2002).
[2] J. G. Bergman, A. Ashkin, A. A. Ballman, J. M. Dziedzic, H. J. Levinstein, and R. G. Smith, Appl. Phys. Lett. **12**, 92 (1968).
[3] E. H. Turner, F. R. Nash, and P. M. Bridenbaugh, J. Appl. Phys. **41**, 5278 (1970).
[4] V. Gopalan, V. Dierolf, and D. A. Scrymgeour, Annu. Rev. Mater. Res. **37**, 449 (2007).
[5] F. Luedtke, K. Buse, and B. Sturman, Phys. Rev. Lett. **109**, 026603 (2012).
[6] A. Riefer, S. Sanna, A. Schindlmayr, and W. G. Schmidt, Phys. Rev. B **87**, 195208 (2013).
[7] D. M. Smyth, Prog. Solid State Chem. **15**, 145 (1984).
[8] S. C. Abrahams and P. Marsh, Acta Crystallogr. Sect. B **42**, 61 (1986).
[9] H. Donnerberg, S. M. Tomlinson, C. R. A. Catlow, and O. F. Schirmer, Phys. Rev. B **40**, 11909 (1989).
[10] F. P. Safaryan, R. S. Feigelson, and A. M. Petrosyan, J. Appl. Phys. **85**, 8079 (1999).
[11] N. Iyi, K. Kitamura, F. Izumi, J. K. Yamamoto, T. Hayashi, H. Asano, and S. Kimura, J. Solid State Chem. **101**, 340 (1992).
[12] A. P. Wilkinson, A. K. Cheetham, and R. H. Jarman, J. Appl. Phys. **74**, 3080 (1993).
[13] H. Nahm and C. Park, Phys. Rev. B **78**, 184108 (2008).
[14] O. F. Schirmer, M. Imlau, C. Merschjann, and B. Schoke, J. Phys.: Condens. Matter **21**, 123201 (2009).
[15] H. Donnerberg, S. M. Tomlinson, C. R. A. Catlow, and O. F. Schirmer, Phys. Rev. B **44**, 4877 (1991).
[16] H. Xu, D. Lee, J. He, S. Sinnott, V. Gopalan, V. Dierolf, and S. Phillpot, Phys. Rev. B **78**, 174103 (2008).
[17] Q. K. Li, B. Wang, C. H. Woo, H. Wang, and R. Wang, J. Phys. Chem. Solid **68**, 1336 (2007).
[18] Y. L. Li, W. G. Schmidt, and S. Sanna, Phys. Rev. B **89**, 094111 (2014).
[19] M. Leslie and M. J. Gillan, J. Phys. C: Solid State Phys. **18**, 973 (1985).
[20] G. Makov and M. C. Payne, Phys. Rev. B **51**, 4014 (1995).
[21] S. Lany and A. Zunger, Phys. Rev. B **78**, 235104 (2008).
[22] C. Freysoldt, C. G. Neugebauer, and J. Van de Walle, Phys. Rev. Lett. **102**, 016402 (2009).
[23] H. P. Komsa, T. T. Rantala, and A. Pasquarello, Phys. Rev. B **86**, 045112 (2012).
[24] P. A. Schultz, Phys. Rev. Lett. **584**, 1942 (2000).
[25] G. Kresse and J. Furthmuller, Comput. Mater. Sci. **6**, 15 (1996).
[26] G. Kresse and J. Furthmuller, Phys. Rev. B **54**, 11169 (1996).
[27] G. Kresse and D. Joubert, Phys. Rev. B **59**, 1758 (1999).
[28] H. J. Monkhorst and J. D. Pack, Phys. Rev. B **13**, 5188 (1976).
[29] J. Heyd, G. E. Scuseria, and M. Ernzerhof, J. Chem. Phys. **118**, 8207 (2003).
[30] A. V. Krukau, A. F. Vydrov, O. A. Izmaylov, and G. E. Scuseria, J. Chem. Phys. **125**, 224106 (2006).
[31] C. Thierfelder, S. Sanna, A. Schindlmayr, and W. G. Schmidt, Phys. Status Solidi C **7**, 362 (2010).
[32] G. C. Van de Walle and J. Neugebauer, J. Appl. Phys. **95**, 3851 (2004).
[33] U. Gerstmann, P. Deák, R. Rurali, B. Aradi, T. Frauenheim, and H. Overhof, in *Proceedings of the 22nd International Conference on Defects in Semiconductors*, Aarhus, 2002 [Physica B **340–342**, 190 (2003)].
[34] F. Gallino, G. Pacchioni, and C. Di Valentin, J. Chem. Phys. **133**, 144512 (2010).
[35] A. Chakrabarty and C. H. Patterson, J. Chem. Phys. **137**, 054709 (2012).
[36] J. F. Janak, Phys. Rev. B **18**, 7165 (1978).
[37] S. Sanna, T. Frauenheim, and U. Gerstmann, Phys. Rev. B **78**, 085201 (2008).
[38] C. Goransson, W. Olovsson, and I. A. Abrikosov, Phys. Rev. B **72**, 134203 (2005).
[39] U. Gerstmann, E. Rauls, H. Overhof, and T. Frauenheim, Phys. Rev. B **65**, 195201 (2002).
[40] O. F. Schirmer, H.-J. Reyher, and M. Wöhlecke, *Insulating Materials for Optoelectronics – New Developments* (World Scientific, Singapore, 1995).
[41] J. Koppitz, O. F. Schirmer, and A. I. Kuznetsov, Europhys. Lett. **4**, 1055 (1987).
[42] A. Savage, J. Appl. Phys. **37**, 3071 (1966).